Noname manuscript No.
(will be inserted by the editor)

Acoustofluidic Interferometric Device for rapid single cell physical phenotyping

J. Mejía Morales · P. Glynne-Jones · M. Vassalli · G.L. Lippi

Received: date / Accepted: date

Abstract High throughput single cell analysis based on physical properties (such as morphology or mechanics) is emerging as a powerful tool to inform clinical research, with a great potential for translation towards diagnosis. Here we present a novel microfluidic approach adopting acoustic waves to manipulate and mechanically stimulate single cells, and interferometry to track changes in the morphology and measure size, deformability, and refractive index of non-adherent cells. The method is based on the integration within the acoustofluidic channel of a low-finesse Fabry-Perot resonator, providing very high sensitivity and a speed potentially suitable to obtain the high throughput necessary to handle the variability stemming from the biological diversity of single cells. The proposed approach is applied to a set of different samples: reference polystyrene beads, algae and yeast. The results demonstrate the capability of the acoustofluidic interferometric device to detect and quantify optomechanical properties of single cells with a throughput suitable to address label-free single cell clinical analysis.

J. Mejía Morales
Université Côte d'Azur, CNRS, INPHYNI, France
Department of Experimental Medicine, University of Genova, 16149 Genova, Italy
Current address: Laboratory of General Biochemistry and Physical Pharmacy, Ghent University, 9000 Ghent, Belgium
E-mail: julian.mejia_morales@ugent.be

P. Glynne-Jones
Engineering Sciences, University of Southampton, SO17 1BJ Southampton, United Kingdom

M. Vassalli
James Watt School of Engineering, University of Glasgow, G12 8LT Glasgow, United Kingdom

G.L. Lippi
Université Côte d'Azur, CNRS, INPHYNI, France

Keywords Microfluidics · Acoustics · Fabry-Perot interferometer · Single cell analysis · Cell mechanics · Cytometry

1 Introduction

The mechanical properties of living cells have been demonstrated to precisely convey information on their physiological condition, reflecting with high accuracy gene expression patterns [1]. As a direct consequence of this connection, the mechanical properties of somatic cells are expected to be a valuable proxy of the phenotype, from very soft, neuronal cell types, to much stiffer, bone and muscle ones [2]. Single cell mechanotyping has proved to be effective in screening for specific cellular conditions [3] and to identify underlying pathological states in patients [4,5]. In addition, the refractive index of cells and tissues has shown the potential for relaying information on the physio-pathological state of biological samples, as it is influenced by the local protein density [6]. At the single cell level, this indicator is particularly effective, and it has been adopted to follow fine intracellular organelle dynamics [7] such as to spot the presence of parasites infecting the cell [8].

Label-free physical indicators of the cellular phenotype, such as mechanics and the refractive index, hold a great promise in the field of personalised medicine [9] and of diagnosis based on single cell analysis [10]. Nevertheless, only a tiny fraction of the proposed methods have been translated towards the clinical research context. The main bottleneck in this process is the low analysis speed typical of standard high resolution single cell techniques, and the need for a paradigm change in the technology to achieve the high throughput re-

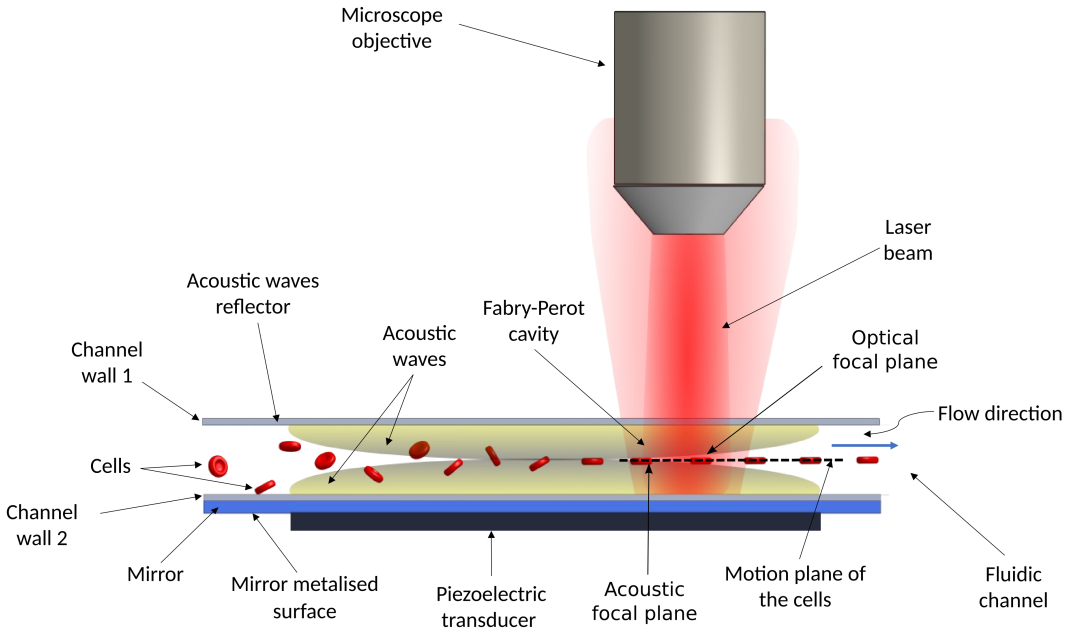

Fig. 1 Elements of the AID. A microfluidic channel producing acoustic manipulation, together with a sketch of the Fabry-Perot resonator used for cytometry. The upper microfluidic channel wall (wall 1) serves as an acoustic reflector and, in addition, as one of the semi-reflective surfaces (mirror equivalent) of the Fabry-Perot interferometer. A piece of second surface mirror is sandwiched between channel wall 2 and the piezoelectric transducer to complete the interferometer. Light is coupled into the resonator using a microscope objective, also used to retrieve the interferometer fringe pattern with the imprinted, cell-induced fringe perturbation. The piezoelectric transducer creates the acoustic waves (yellow to black gradient) to focus the cells (red blood cells in the schematics) into a single motion plane.

quired to cope with the biological diversity [11]. High throughput is normally achieved by means of microfluidics, where cells are driven through the analysis module one by one at very high flow rates (up to 100-1000 cells/s) and in recent years high throughput label-free cytometry devices have been proposed to access mechanical [12] or refractive index [13] information of single cells.

In this contribution, we present an Acoustofluidic Interferometric Device (AID) aimed at simultaneously measuring single cell optical and mechanical properties with high throughput. The AID is based on a microfluidic chip where acoustic standing waves are used to first levitate, then squeeze [14] single cells in the channel [15] to probe their mechanical properties. Moreover, we integrated a Fabry-Perot interferometer into the same channel, so that the deformation and size of the cells can be precisely monitored in real-time through the optical fringe changes, thereby collecting a signal that integrates information on the cell's physical (deformation) and optical (refractive index) properties.

2 Materials and methods

The AID is endowed with a cell acoustic manipulation system (see Fig. 1). For this purpose, the microfluidic channel is equipped with a piezoelectric transducer that allows for cell acoustic focusing and deformation. When the acoustic standing wave is active, the focused cells move at constant speed in the plane of the acoustic field pressure node. Flowing along the channel, the cells traverse the region illuminated by the laser, which forms a plano-planar Fabry-Perot interferometer, and perturb its interference pattern (cf. Fig. 2). The interferometer's fringe pattern - in the presence or in the absence of a cell - is retrieved through the same microscope objective used to couple light into the resonator. The retroreflected light is then redirected towards the detection unit (cf. Fig. 3), where the fringe pattern is processed to retrieve the Finesse and the Cell Focal Length (CFL), parameters related to the Young modulus and to the Refractive Index (RI), as detailed in the Supplementary Material.

When an acoustically focussed cell crosses the AID's Fabry-Perot cavity it perturbs the resonator fringe pattern (mathematically described by the Airy transmission function) [16,17]. We have identified two types of

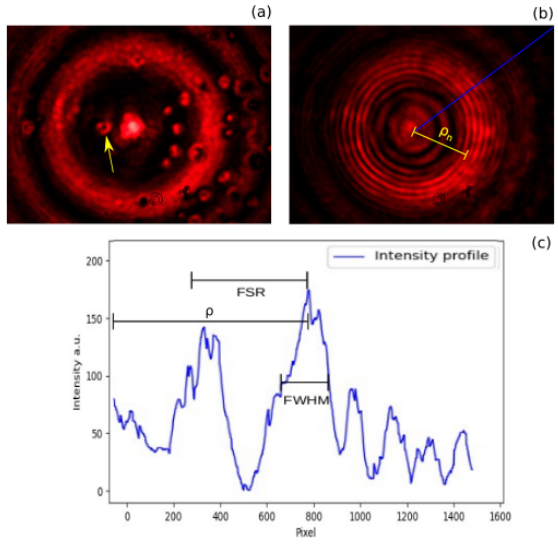

Fig. 2 Panel (a): Yeast cell (yellow arrow) crossing the resonator off-axis, thus weakly interacting with the background fringe pattern. Panel (b): Yeast-induced strong perturbation of the fringe pattern (same cell pointed in panel (a)), due to cell positioning on the resonator's axis. The fringe pattern of the low finesse Fabry-Perot resonator is recognizable in the background of both panels. The distance from the center to the n-th intensity fringe is identified by the parameter ρ_n. Panel (c): The intensity profile of the image plotted over the radial line (blue line) shown in panel (b). The intensity profiles are used to retrieve the parameters ρ, FSR and the FWHM used to asses the cell optomechanical properties.

cell-induced perturbations: strong and weak. The first occurs when the cell crosses the optical resonator's axis, while the second takes place when the cell crosses any other portion of the resonator (cf. Figs. 2 panel (a) and (b)). Since the strong perturbations are better defined and easier to observe, we concentrate on this choice and report on the strong Cell-induced Fringe Pattern Perturbations (CFPP) analyzed by means of the Finesse and CFL parameters.

2.1 Finesse

The Finesse $\mathcal{F}$, eq. (1), is the ratio between the Free Spectral Range (FSR) and the Full Width at Half Maximum (FWHM) of the CFPP (cf. Fig. 2 (c)). This is an important parameter emerging from the mathematical expression for the resonator's transmitted irradiance defined by the so-called Airy transmission function [18]. Notably, the Finesse is also related to the reflection coefficients of the reflective surfaces that form the Fabry-Perot cavity [17].

$$\mathcal{F} = \frac{\mathrm{FRS}}{\mathrm{FWHM}}\,. \tag{1}$$

2.2 Cell Focal Length

The CFPP can be modeled as a modification of the Fabry-Perot's resonator fringe pattern induced by a thin lens [15] (cf. Supplementary Material). The mathematical model used to describe the cell-resonator interaction is developed using propagation ray-matrices and is based on the ρ parameter (cf. Fig. 2 (b)). The distance from the center to a bright fringe is ρ_n while the next bright fringe distance is ρ_{n+1}. These distances are used to compute the radius of curvature of the wavefront exiting the resonator (cf. Supplementary Material) which interferes with the incoming laser beam focussed by the microscope objective (cf. Fig. 1). Since the cell is modelled as a thin lens, it is possible to associate a focal length to the cell (cf. Supplementary Material). The CFL and the Finesse (based on FWHM and FSR) are the parameters used to summarize and analyze the cell optomechanical properties. The interferogram analysis used to retrieve the Finesse and CFL from the CFPP is also applicable to the intrinsic fringe pattern of the resonator without cells. Moreover, the results reported in section 3 relates only to the Finesse and CFL of the CFPP since these parameters allows for cells' optomechanical properties retrieval.

2.3 AID construction details

The microfluidic chip used in this work is an acoustic planar half-wave resonator constructed in a similar manner to our previous work, but with a revised sequence of layer thicknesses to support a thinner channel height. [19,20]. A 5mm wide channel was laser-cut into a single layer of double-sided adhesive transfer tape sheet (106 μm thick 468MP, 3M, USA). The 35 $\times$ 50 mm transfer tape was sandwiched between two microscope cover slips (170 μm thick, 25 $\times$ 75 mm, 0CON-161, Logitech, Glasgow, UK) to create the microfluidic channel walls; a second surface, fully reflecting mirror (35 $\times$ 50 mm and 4 mm thickness, edmund optics, UK) is attached to the back microscope cover slip. Access holes (diameter 1 mm) to the microchannel are drilled at both ends of the channel (see Fig. 1 and [19]).

Under a portion of the fluid channel, a piezoelectric transducer of lead zirconate titanate (PZ-26, Ferroperm, Kvistgaard, Denmark) is attached with epoxy (Epotek-301, Epoxy Technology, Inc., USA). The transducer is (1mm x 25mm x 35mm) in size, and a wrap-around electrode is created on the top surface to allow electrical contact to both sides using conductive silver paint (SCP Silver Conductive Paint, Electrolube Ltd.,

UK).

A Direct Digital Synthesizer (DDS) AD9850 drives the piezoelectric transducer and is controlled by a Raspberry Pi 3 in conjunction with a custom-built amplifier based on a high-frequency op-amp (LT1210). The driving frequency is tuned to the microfluidic's channel fundamental acoustic mode resonance (6.682 MHz) with amplitude 15 V_{pp} for acoustic focussing, and 25 V_{pp} for cell deformation.

At the air-wall interface (channel wall 1 in Fig. 1) the intensity reflection coefficient is $r_1 = 0.04$, while at the back mirror we have $r_2 = 0.9$, leading to a coefficient of finesse $F = 0.15$ and to a Finesse $\mathcal{F} = 0.6$. This value is quite low ($\mathcal{F}$ ranges at least above 10, and often over 100 in common interferometers), whence the identification "low-Finesse" for our device. The low-Finesse configuration, provided by the large-gap Fabry-Perot interferometer (channel width L much larger than the cell diameter ℓ: $L \geq 10 \times \ell$), has been chosen for its high throughput potential in optomechanical properties-based cytometry. Indeed, it offers better flexibility for the integration of the cells' acoustic manipulation. In contrast, high-Finesse configurations require a holder for correctly positioning the cell inside the resonant cavity [21] . A high-Finesse configuration is incompatible with high throughput, in addition to presenting difficulties in the implementation of the acoustic focusing. In fact, a fringe shift measurement requires high stability at the interferometric level, necessitating, on the one hand, continuous calibration (e.g., for changes in pressure inside the microfluidic channel) and, on the other hand, excellent overall mechanical stability. These requirements render the choice of a high-Finesse configuration impractical for an instrument whose vocation is flexibility and ease of use.

A simple hydrostatic pressure system is created using a pair of 10 ml tubing-connected syringes to induce and control the flow inside the microfluidic channel. This system permits the generation of pressure values between 100 and 3000 Pa, thus inducing cell speeds in the range $v_c = 50 - 180$ μm/s. The most common operation values used in experiments are around 16 μl/min for the flow rate, i.e., an equivalent speed of $v_c = 60$ μm/s.

2.4 Detection unit

A Thorlabs non-polarizing beamsplitter (BSN10 – optical Anti-Reflection coating: 400-700 nm), is used in combination with the microscope objective (20X, Nikon

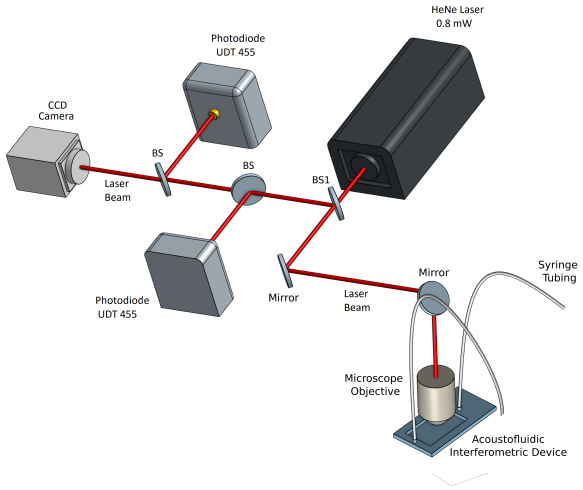

Fig. 3 A He-Ne laser use used as a light source for the microfluidic chip. The laser beam is directed to the microscope objective through beamsplitter BS1 and two steering mirrors and is coupled into the resonator by the microscope objective. The reflected Fabry-Perot fringe pattern is retrieved by the (infinite conjugate) objective and directed, through the same steering mirrors and additional beamsplitters, to the two photodiode detectrs (UDT-455)and to the CCD camera for data analysis.

CFI Plan Fluor) to couple light into the acoustofluidic channel and to retrieve the fringe pattern with or without the perturbation caused by the cell (Fig. 3). The He-Ne laser (Thorlabs, HNLS008L-EC) beam carrying the CFPP is directed onto a CCD: an acA1600-20gm Basler camera with 12-bit resolution and a sensor of dimensions 1626 px × 1236 px. The pixel size is 4.4 μm × 4.4 μm. In addition, the Resonator Fringe Pattern (RFP) carrying laser beam is split into two branches using two beamsplitters (BS) and directed to two UDT-455 (OSI Optoelectronics) photodiodes as shown in Fig 3.

It is worth noticing that the spot size of the laser beam focussed by the microscope objective at the first surface of the Fabry-Perot resonator is $\approx 4\,\mu$m. The small spot size enables the use of inexpensive parts such as a second surface mirror and a coverslip to create the Fabry-Perot resonator. Such low optical quality elements could not produce a good fringe pattern even in low Finesse systems if the laser beam were broad.

The two diode detectors are aligned to detect the fringe pattern perturbation at two different points along the cell path inside the microfluidic channel, allowing for cell speed measurement. The one-dimensional nature of the time traces acquired with the photodiode detector is suitable for real-time analysis. At the same time, the 2D camera images are useful for CFPP sta-

tistical analysis and for acoustophoretic plane identification.

2.5 Samples

The samples used to test the AID operation are algae (*Tetraselmis* sp.), yeast (*Saccharomyces cerevisiae*) and polystyrene beads with diameter $d_p = 3$ μm purchased from Polysciences Inc. The algae have neither a peculiar cell membrane nor a particular cytoskeleton structure, thus are expected to be quite elastically compliant [22]. The cell wall's Young modulus (E) for yeast is ($E \approx 112 \pm 6$) MPa [23], while its value for the whole cell is expected to be in the kPa range. The Young modulus of the polystyrene beads is $E = 3.25$ GPa [24]. Based on the respective Young's moduli, we can rank our samples in the following order (from the most to the least elastically compliant): algae, yeast, and polystyrene beads. This order matches the results of our observations, as we see in the following section.

2.6 Experimental procedure

In order to demonstrate the working principle behind the AID it is operated at low throughput to obtain the CFPP images of the levitated and acoustically deformed cells as follows: 1. the flow inside the microfluidic channel is stopped when a cell is aligned with the resonator's axis (while acoustically focussed); 2. the interference pattern resulting from the immobile and levitated cell is then acquired, obtaining the information in the absence of deformation (Fig. 4 (a)); 3. the acoustic wave's amplitude is increased to induce a cell deformation and a new image of the interference pattern is acquired (Fig. 4 (b)). The cycle is repeated to obtain 20 pairs of patterns for each cell (or polystyrene bead) in the absence and in the presence of deformation.

The primary acoustic field is predicted to be of order 500 kP a, with associated (oscillating) acoustic displacements of a few nm. These displacements are thus small (and insignificant) in comparison to the cell deformation likely to be created from the non-zero time averaged acoustic radiation force. In our previous work (albeit in a different system with higher pressure amplitudes) [14] these were of order 15 kPa, and resulted in cell wall displacements of a few μm.

The images captured with the CCD are analysed by converting each image in a set of 360 intensity profiles obtained by taking radial cuts every degree, similar to the one displayed in Fig. 2 (c). In order to do so, the images are converted to polar coordinates to obtain the 360 independent intensity radial cuts through the image. Then, the profiles are computationally analyzed to obtain the parameters: ρ, FWHM, and FSR. An outlier elimination procedure is implemented to improve the normality of our dataset [15]. The statistical significance of the resulting estimates is analyzed with Student's T-test [25]. Finally, a weighted average (with the standard deviation of the parameters as a weight) of ρ, FWHM and Finesse, and the CFL is computed. The corresponding results are shown in Fig. 5.

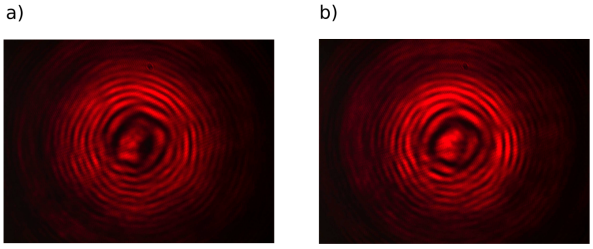

Fig. 4 Example of the images used to retrieve the ρ, Finesse, and FWHM for the AID analysis. Panel (a): Algae cell acoustically levitated. Panel (b): cell acoustically levitated and deformed. By direct comparison it is not possible to establish an optical difference nor to identify which one is the image that corresponded to the acoustic deformation. Only through the AID analysis it is possible to retrieve the optomechanical information present in panels (a) and (b), as shown in the results.

3 Results and discussion

Results show an acoustically-induced cell deformation for yeast and algae. A matching reduction in Finesse and CFL values is also observed. The polystyrene beads, instead, do not present a significant deformation, as expected, given that their Young's modulus is approximately five orders of magnitude larger.

The CFL computation mainly depends on the optical thickness of the cell inside the FP resonator while the Finesse is also sensitive to the global stability of the cell-resonator ensemble. The latter changes as the cell shape does, thus engendering a more complex dependence between cell deformation and Finesse. Hence, while both parameters will provide information about Young's modulus, refractive index and cell shape (optomechanical properties), the CFL gives a more readily interpretable result (cf. Supplementary Material).

The more direct dependence of the CFL on cell features is the likely source of the better statistical significance obtained from the CFL, even though a qualitative agreement between expected deformability and

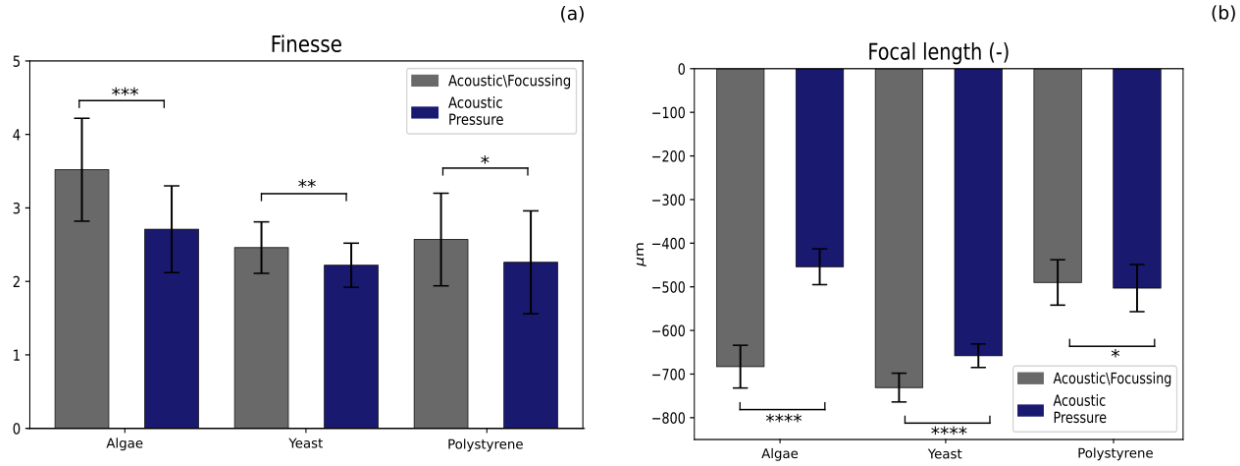

Fig. 5 Effect of acoustic pressure on samples with different optomechanical properties measured with the Finesse and CFL parameters. (a) Finesse values for tetraselmis (algae), Saccharomyces cerevisiae (yeast), and polystyrene beads 3 μm diameter. (b) CFL values for tetraselmis (algae), Saccharomyces cerevisiae (yeast), and polystyrene beads 3 μm diameter. Gray bars represents acoustic focusing, while blue bars display the results for acoustic deformation. The asterisks in the plots indicate the statistical significance as follow: **** $P< .0001$, *** $P< .001$, ** $P< .05$ and * $P> .1$. The P-scores were computed from the samples T-test results.

interferometric characterization of the measured samples is obtained for both parameters.

It is worth noticing that the theoretical model implies two solutions for the CFL (cf. Supplementary Material eqs. (31) and (32)). The question arises as to whether the negative sign for the lens focal length is justified in 5 (b). Here, we have to keep in mind that due to the very low cavity Finesse, we are not modelling (or even using) a true Fabry-Perot resonator but, rather, a two-beam interferometer (low-Finesse resonator, cf. section 2.3). Thus, the presence of the cell, through the increase in optical path length, increases the distance from which the image of the incoming beam is seen, mimicking the effect of a negative (divergent) lens. The sign is therefore consistent with expectations.

Finally, it is important to remark that the value of the CFL of the polystyrene microspheres should not be interpreted as a true focal length, matching the bead's refraction, but rather as a general indicator to be used for comparison between the focussing and deformation conditions. The reason for this resides in the material's index of refraction – much larger than the one of the surrounding medium, at variance with all cells –, which leads to a thick lens with very short focal length, violating the conditions for the model. Our choice of using, nonetheless, the thin lens model for these data stems from the need for treatment consistency. Thus, the results for the microspheres hold significance in the comparison between the low and high pressure: the lack of statistical difference between the two cases is the proof for the non-deformability of the microspheres and for the ability of the system to detect this fact, even though the mathematical conditions for the parameter reconstruction are not met.

4 Conclusions

Here we presented a novel acoustofluidic cytometry device integrating a low-Finesse Fabry-Perot resonator, the AID. The Finesse of the cavity and the reconstructed Cell Focal Length convey information on the physical properties of the cell, such as the mechanical properties, the refractive index and the shape. This instruments is capable of detecting deformations in the cell shape when acoustic pressure is applied with a resolution not achievable with a standard imaging approach (see Fig. 4). Therefore, the AID enables the high throughput measurement of the mechanical properties of cells in a regime of low deformations, closer to physiological stimuli, and not accessible to existing mechanical cytometry techniques.

The results of Fig. 5 demonstrate the utility of the thin-lens approach. A quantitative match between measured focal lengths and cell deformation state will be addressed in future work. For this purpose, a new instrumental design is being developed to permit the acquisition of very large amounts of data for statistical analysis. We also foresee that a line-focused resonator will allow better alignment between the laser spot and the cells.

The proposed AID device offers a novel perspective on the physical phenotyping of single cells, where me-

chanics is one aspect, but a more detailed - possibly AI-driven - analysis of the complex deformation of the optical cavity induced by the passage of the cell is expected to provide additional and more specific information. The potential of the technique, together with the limited manufacturing cost, sets the AID as a promising approach for next generation high throughput single-cell physical cytometry, with applications in basic research and medical diagnosis.

Acknowledgements The authors would like to thank: Dr. Marco Sartore (ElbaTech SRL) for the support provided with the experiment's electronics; Dr. Chiara Gambardella (National Research Council, Genova, Italy) for providing the Tetrasl mis samples; Dr. Stéphane Barland (UCA Nice), Prof. Dr. Jochen Guck (Max Planck Institute for the Science of Light) and Dr. Salvatore Girardo (Biotechnology Center - Technische Universität Dresden) for fruitful discussions. J.M.M. acknowledges support from the Mexican Council of Science and Technology (CONACyT) for financial support (Scholarship No. 471712) and funding for international mobility France–Italy provided by the Université Franco Italienne (UFI, Project No.C2-1031). In addition, thanks are due to Prof. Dr. Kevin Braeckmans and Prof Dr.Stefaan De Smedt (LGBPP Ghent University) for current support. PGJ gratefully acknowledges fellowship funding by the UK EPSRC (No. EP/L025035/1). This work has also been supported by the French government through the UCAJEDI Investments in the Future project managed by the National Research Agency (ANR) with Reference No. ANR-15-IDEX-01.

References

1. Marie F. A. Cutiongco, Bjørn Sand Jensen, Paul M. Reynolds, and Nikolaj Gadegaard. Predicting gene expression using morphological cell responses to nanotopography. *Nature Communications*, 11, 03 2020.
2. Jochen Guck. Some thoughts on the future of cell mechanics. *Biophysical Reviews*, 11:667–670, 09 2019.
3. Yusuke Toyoda, Cedric J. Cattin, Martin P. Stewart, Ina Poser, Mirko Theis, Teymuras V. Kurzchalia, Frank Buchholz, Anthony A. Hyman, and Daniel J. Müller. Genome-scale single-cell mechanical phenotyping reveals disease-related genes involved in mitotic rounding. *Nature Communications*, 8:1266, 11 2017.
4. Yuri Belotti, Serenella Tolomeo, Michael J. Conneely, Tianjun Huang, Stephen J. McKenna, Ghulam Nabi, and David McGloin. High-throughput, time-resolved mechanical phenotyping of prostate cancer cells. *Scientific Reports*, 9:5742, 04 2019.
5. Markéta Kubánková, Bettina Hohberger, Jakob Hoffmanns, Julia Fürst, Martin Herrmann, Jochen Guck, and Martin Kräter. Physical phenotype of blood cells is altered in covid-19. *Biophysical Journal*, 120(14):2838–2847, 2021.
6. Zhuo Wang. Tissue refractive index as marker of disease. *Journal of Biomedical Optics*, 16:116017, 11 2011.
7. Patrick A. Sandoz, Christopher Tremblay, F. Gisou van der Goot, and Mathieu Frechin. Image-based analysis of living mammalian cells using label-free 3d refractive index maps reveals new organelle dynamics and dry mass flux. *PLOS Biology*, 17:e3000553, 12 2019.
8. YongKeun Park, Monica Diez-Silva, Gabriel Popescu, George Lykotrafitis, Wonshik Choi, Michael S. Feld, and Subra Suresh. Refractive index maps and membrane dynamics of human red blood cells parasitized by plasmodium falciparum. *Proceedings of the National Academy of Sciences*, 105:13730–13735, 09 2008.
9. Julia M. Hillger, Wai-Ling Lieuw, Laura H. Heitman, and Adriaan P. IJzerman. Label-free technology and patient cells: from early drug development to precision medicine. *Drug Discovery Today*, 22:1808–1815, 12 2017.
10. Thomas R. Carey, Kristen L. Cotner, Brian Li, and Lydia L. Sohn. Developments in label-free microfluidic methods for single-cell analysis and sorting. *Wiley Interdisciplinary Reviews: Nanomedicine and Nanobiotechnology*, 11:e1529, 04 2018.
11. Eric M. Darling and Dino Di Carlo. High-Throughput assessment of Cellular Mechanical Properties. *Annu. Rev. Biomed. Eng*, 17:35–62, 2015.
12. Oliver Otto, Philipp Rosendahl, Alexander Mietke, Stefan Golfier, Christoph Herold, Daniel Klaue, Salvatore Girardo, Stefano Pagliara, Andrew Ekpenyong, Angela Jacobi, Manja Wobus, Nicole Töpfner, Ulrich F. Keyser, Jörg Mansfeld, Elisabeth Fischer-Friedrich, and Jochen Guck. Real-time deformability cytometry: on-the-fly cell mechanical phenotyping. *Nature Methods*, 12:199–202, 03 2015.
13. Dhananjay Kumar Singh, Caroline C. Ahrens, Wei Li, and Siva A. Vanapalli. Label-free, high-throughput holographic screening and enumeration of tumor cells in blood. *Lab on a Chip*, 17:2920–2932, 08 2017.
14. Puja Mishra, Martyn Hill, and Peter Glynne-Jones. Deformation of red blood cells using acoustic radiation forces. *Biomicrofluidics*, 8(034109):1932–1058, 2014.
15. Julián Mejía Morales. *Acoustofluidic interferometric device for optomechanical cytometry.* PhD thesis, Université Côte d'Azur and Università di Genova, 2021, https://tel.archives-ouvertes.fr/tel-03253494/document.
16. F.A. Jenkins and H.E. White. *Fundamentals of Optics*. McGraw-Hill, 1950.
17. Max Born and Emil Wolf. In *Principles of Optics*. Pergamon, 6th edition, 1980.
18. Julia Casanueva Diaz. Fabry-Perot cavities in advanced virgo. *Control of the Gravitational Wave Interferometric Detector Advanced Virgo*, pages 37–83, 2018.
19. Peter Glynne-Jones, Rosemary J. Boltryk, and Martyn Hill. Acoustofluidics 9: Modelling and applications of planar resonant devices for acoustic particle manipulation. *Lab on a Chip*, 12:1417–1426, 04 2012.
20. Robert Zmijan, Umesh S. Jonnalagadda, Dario Carugo, Yu Kochi, Elizabeth Lemm, Graham Packham, Martyn Hill, and Peter Glynne-Jones. High throughput imaging cytometer with acoustic focussing. *RSC Adv.*, 5:83206–83216, 2015.
21. W. Z. Song, X. M. Zhang, A. Q. Liu, C. S. Lim, P. H. Yap, and Habib Mir M. Hosseini. Refractive index measurement of single living cells using on-chip fabry-pérot cavity. *Applied Physics Letters*, 89:203901, 11 2006.
22. Antonio Nava. Graduate studies modeling of growth kinetics and characterization of membrane modeling of growth kinetics and characterization of membrane mechanics mechanics, *University of Denver*, 2012.
23. Alexander E. Smith, Zhibing Zhang, Colin R. Thomas, Kennith E. Moxham, and Anton P. J. Middelberg. The mechanical properties of saccharomyces cerevisiae. *Proceedings of the National Academy of Sciences*, 97:9871–9874, 08 2000.

24. Dan Guo, Jingnan Li, Guoxin Xie, Yuanyuan Wang, and Jianbin Luo. Elastic properties of polystyrene nanospheres evaluated with atomic force microscopy: Size effect and error analysis. *Langmuir*, 30:7206–7212, 06 2014.
25. C. Alan Boneau. The effects of violations of assumptions underlying the t test. *Psychological Bulletin*, 57:49–64, 1960.